

Supplementary Information

Exciton Migration in Multi-Stranded Perylene Bisimide J-Aggregates

*Chris Rehhausen¹, Matthias Stolte², Stefanie Herbst², Markus Hecht², Stefan Lochbrunner¹,
Frank Würthner^{2*}, and Franziska Fennel^{1*}*

¹Institute for Physics and Department “Life, Light & Matter”, University of Rostock, 18051
Rostock, Germany

²Institut für Organische Chemie & Center for Nanosystems Chemistry, Universität Würzburg,
Am Hubland, 97074 Würzburg, Germany

Content

S1. Experimental details.....	3
S1.1 UV/VIS & Fluorescence measurements	3
S1.2 Pump-Probe measurements	3
S2. Aggregation studies.....	5
S3 Liquid crystalline phase	6
S4. Atomic Force Microscopy (AFM)	7
S5. Determination of the exciton coupling by means of the vibrational progression in the absorption	8
S6. Determination of the coherence length	10
S6.1 Determination of the Huang-Rhys factor	10
S6.2 Coherence length from the vibrational progression in the emission.....	13
S6.3 Coherence length from motional narrowing	15
S7. Comparison of transient spectra.....	17
S8. Exciton diffusion properties.....	18
S8.1 Determination of the excitation density	18
S8.2 Determination of the diffusion constant.....	19
S9. Lifetime measurements	21
S10. Spectral overlap of absorption and emission	22

S1. Experimental details

S1.1 UV/VIS & Fluorescence measurements

For the measurement of the UV/vis absorption spectra a Specord 50 absorption spectrometer (Analytical Jena) was used, if not denoted otherwise. The fluorescence was measured with a FluoroMax-4P spectrofluorometer (Horiba Scientific) and corrected for the wavelength dependent detection sensitivity. The absorption was measured in the same 420 μm thick cuvette as used for the transient absorption measurements. In the fluorescence measurements the samples are excited at 595 nm. In order to avoid self-absorption, the samples were diluted by a factor of four compared to the concentration of the transient absorption measurements and measured in a 200 μm cuvette. Thus the maximum of the absorption was less than 0.05 OD. The dilution changed the absorption spectra of **PBI1-Me** only slightly. For **PBI1** there was a contribution of the monomer visible in the spectrum after dilution, but the contribution of the aggregate was still dominating. By choosing a proper excitation wavelength the aggregates could be excited selectively to avoid any contamination from the monomer fluorescence. The dark signal was measured with the pure solvent and subtracted.

The UV/vis measurements for the aggregation studies and the absorbance in LC phase were measured with a Perkin Elmer Lambda 950. The quantum yields were measured at room temperature on an Edinburgh Instruments FLS980-D2D2-ST spectrometer under magic angle conditions (54.7°) with a front face sample holder F-J03 and were corrected against the photomultiplier sensitivity as well as the lamp intensity. Solvents (spectroscopic grade, Uvasol®, Merck) and commercially available quartz cuvettes (Hellma) of the passage length 1 cm to adjust OD <0.05 were used.

S1.2 Pump-Probe measurements

The setup for the transient absorption measurements is based on a regenerative Ti:sapphire laser system (CPA 2001, Clark MXR) providing NIR pulses with a duration of 180 fs, a center wavelength of 775 nm, and a repetition rate of 1 kHz. A non-collinearly phase-matched optical parametric amplifier [1] pumped by the Ti:sapphire system is applied to generate excitation pulses centered at 600 nm (560 nm for the streak camera measurements). The pulses are compressed with a fused silica prism sequence to a duration of 25 fs. As probe light serves a white light continuum generated in a 4 mm thick calciumfluoride substrate pumped with a small fraction of the Ti:sapphire output. The time delay between the pump and the probe pulse is adjusted by a retro reflector on a motorized

delay stage in the excitation beam path. Behind the sample, the white light is spectrally resolved by a fused silica prism and detected with a photodiode array. The polarization angle between pump and probe pulse is set to the magic angle (54.7°) by an achromatic half wave plate. The intensity of the pump pulse is adjusted by a wire-grid polarizer. The sample is prepared in a 420 μm thick cuvette with a ultrathin window in order to avoid prolongation of the pulses.

S2. Aggregation studies

A stock solution of high concentration in methylcyclohexane (**PBI1**: $c_0 = 3.85 \times 10^{-4} \text{ mol L}^{-1}$, **PBI1-Me**: to $2.50 \times 10^{-4} \text{ mol L}^{-1}$) is step-wise diluted at 20 °C in order to investigate the absorption depending on the concentration. The dissociation of J-aggregates is indicated by the color change of the sample from blue to red and by the hypsochromic shift of the main absorption band from 620 nm (aggregate) to 563 nm (monomer in MCH) for **PBI1** and from 651 nm (aggregate) to 571 nm (monomer in MCH) for **PBI1-Me** (data are displayed in Fig. 2 in the main manuscript). The concentration-dependent data are in accordance with a cooperative nucleation-elongation growth mechanism, thereby leading to instantaneous aggregate growth into extended nanofibers in a narrow concentration regime. We used the Goldstein-Stryer nucleation-elongation model [2] in order to determine the nucleation constant K_N , the elongation constant K_E and the cooperativity factory $\sigma = K_N/K_E$. These parameters are summarized in Tab. S2.1. The aggregation processes can be described nicely by this model, which can be seen in the inset of Fig. 2b in the main text. There the fraction of aggregated molecules $\alpha_{\text{agg}} = 1 - \alpha_I / \alpha_T$ is plotted depending on $K_E \cdot c_T$ assuming a nucleus size of two.

Tab. S2.1 Fitting parameter K_N and K_E from Fig. S1.2 and the cooperativity factor σ .

	K_E [L mol ⁻¹]	K_N [L mol ⁻¹]	σ
PBI1	120,000	12	0.0001
PBI1-Me	1,350,000	270	0.0002

The spectral parameters like extinction maximum, aggregation induced shift and central wavelength for monomer in CH₂Cl₂ and aggregate in MCH are given in Tab. S1.2.

Tab. S2.2 Spectroscopic properties of **PBI1** and **PBI1-Me** determined by UV-Vis absorption measurements of the monomers in CH₂Cl₂ and aggregates in MCH.

PBI	Monomer (in CH₂Cl₂)^a		Aggregate (in MCH)^b			
	λ_{abs} [nm]	ϵ [L mol ⁻¹ cm ⁻¹]	λ_{abs} [nm]	ϵ [L mol ⁻¹ cm ⁻¹]	$\Delta\tilde{\nu}_{\text{Agg-Mon}}$ [cm ⁻¹]	μ_{eg} [D]
PBI	564	34,100	620	60,700	-1600	6.6
1-Me	571	44,100	651	77,200	-2150	7.1

^a CH₂Cl₂ ($c_0 = 1.2 - 1.9 \times 10^{-5} \text{ mol L}^{-1}$) at 25 °C; ^b MCH ($c_0 = 10^{-4} - 10^{-5} \text{ mol L}^{-1}$) at 20 °C

The minor differences in the molar extinction coefficient (ϵ_{\max}) of the monomer in DCM as well as the transition dipole moment (μ_{eg}) can be presumably associated with the reduced flexibility of the bay substituents for **PBI1-Me** and the associated rigidification of the PBI chromophore (Table S2.2). Additionally, we observe a small shift in the spectral position of the $S_0 \rightarrow S_1$ absorption maximum between **PBI1** (564 nm) and **PBI1-Me** (571 nm) of the monomer in DCM. Minor differences in the vibrational progression are also present. Nevertheless, both monomers have very comparable Huang-Rhys factors of 0.67 (**PBI1**) and 0.66 (**PBI1-Me**), for details see Tab. S5.1 in the SI.

S3 Liquid crystalline phase

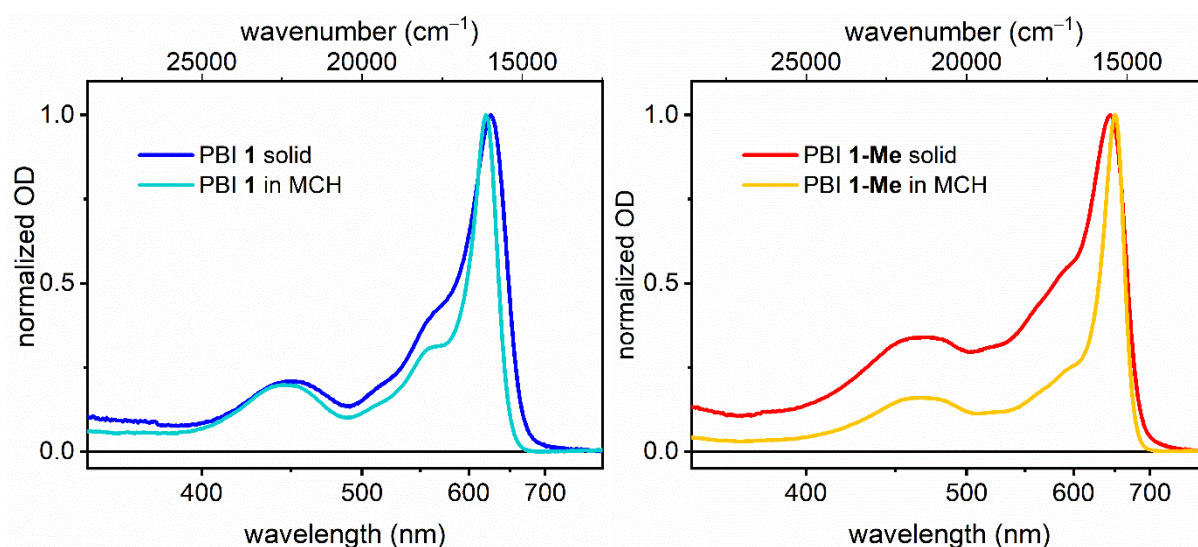


Fig. S3. Normalized absorption spectra of the aggregates in MCH and in liquid crystalline phases.

S4. Atomic Force Microscopy (AFM)

AFM measurements were performed under ambient conditions using a silica cantilever with a resonance frequency of ~ 150 kHz and a spring constant of ~ 10 Nm^{-1} . Samples were prepared by spin-coating of a methylcyclohexane solution ($c \sim 10^{-5}$ M) onto silicon wafer (Si-wafer) with 2000 rpm. The aggregates were investigated in tapping mode. Via the cross section analysis of the aggregates along a certain distance perpendicular to the aggregates the height of the nanofibers were determined as 1.9 ± 0.1 nm for **PBI1-Me** and 2.4 ± 0.1 nm for **PBI1**, respectively (Figure S2). Although a tendency of increasing heights could be observed, these experiments are not suited to distinguish the exact number of PBI strands within the aggregate fiber.

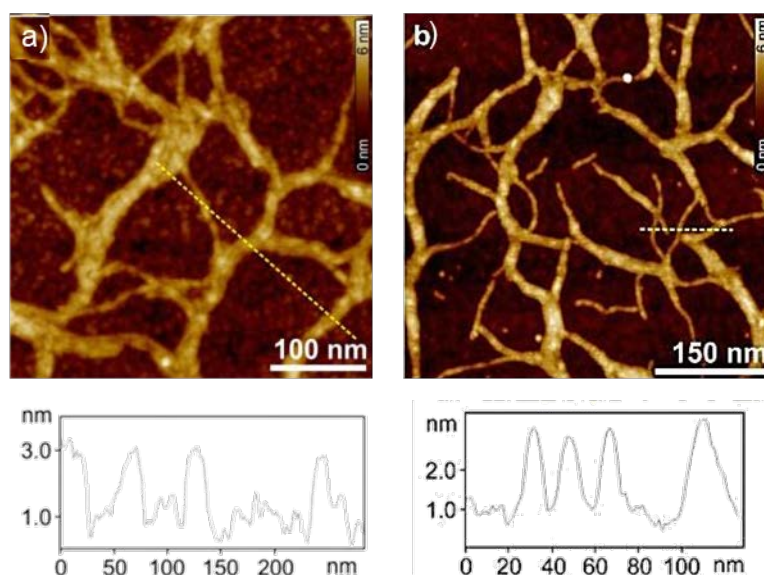


Fig. S4. Height AFM images (top) and cross-section analysis (bottom) of a) **PBI1** and b) **PBI1-Me** prepared by spin-coating of MCH solutions ($c \sim 10^{-5}$ M) on silicon wafer. The cross-section analysis was performed for the dashed yellow lines in the images and the Z scale is 6 nm. Co-agglomeration of the aggregates leads to the formation of bundles and a network-like structure of aggregates of up to several hundred nanometers in length.

S5. Determination of the exciton coupling by means of the vibrational progression in the absorption

The vibronic peak ratio $\frac{a_1}{a_2}$ of the aggregate absorption with the 0-0 transition intensity a_1 and the 0-1 transition intensity a_2 increases for increasing electronic coupling of a dimer according to

$$\frac{a_1}{a_2} = \frac{1}{HR} \left[\frac{1 + \frac{G(0, HR)e^{-HRJ}}{\Delta\nu}}{1 + \frac{G(1, HR)e^{-HRJ}}{\Delta\nu}} \right]^2 \quad (\text{S5.1})$$

where HR is the Huang-Rhys factor of the monomer, $\Delta\nu$ is the vibrational frequency of the monomer, $G(v, HR)$ is the vibrational function, see below, and J is the electronic coupling [3, 4].

The vibrational function $G(v, HR)$ reads

$$G(0, HR) = \sum_{u=1}^{\infty} \frac{HR^u}{u! * u} \quad \text{and} \quad G(1, HR) = \sum_{u=2}^{\infty} \frac{HR^u}{u! * (u-1)} - 1 \quad (\text{S5.2})$$

Due to the small differences in the HR-factor we consider an HR factor of 0.66 for both PBIs. The resulting vibrational functions are $G(0, 0.66) = 0.79$ and $G(1, 0.66) = -0.76$. The calculated peak ratio (as calculated with Eq. S5.1) for the given HR factor of 0.66 and a vibrational frequency of $\Delta\nu = 1330 \text{ cm}^{-1}$ is plotted as function of the electronic coupling in Fig. S5.2 as black line.

The measured absorbance is divided by $\tilde{\nu} = 1/\lambda$ before analyzing the peak ratio. This converts the oscillator strength into the density of states [5]. For both PBIs, fitting the aggregate absorption by Gaussian bands is only possible with low quality due to the overlap of the first and second excited state and the asymmetric line shapes. Therefore, we estimate the peak ratio by reading the values for the a_2 intensity directly from the frequency corrected and to the a_1 peak normalized absorbance as given in Fig. S5.1. The intensity of the a_2 peak is determined as the absorbance at a wavenumber blue shifted from the 0-0 peak by the vibrational frequency of the monomer as given in Tab. S6.1. The resulting values of 0.29 and 0.24 are marked in Fig. S5.1. The peak ratio is the inverse. It is given in Tab S5.1 and the aggregates is marked in Fig. S5.2 as green horizontal line for **PBI1** and as red line for **PBI1-Me**. The intersections between the horizontal lines and the peak ratio calculated by Eq. S5.1 give the respective electronic coupling which can be read of the x-axis and are listed in Tab. S5.1.

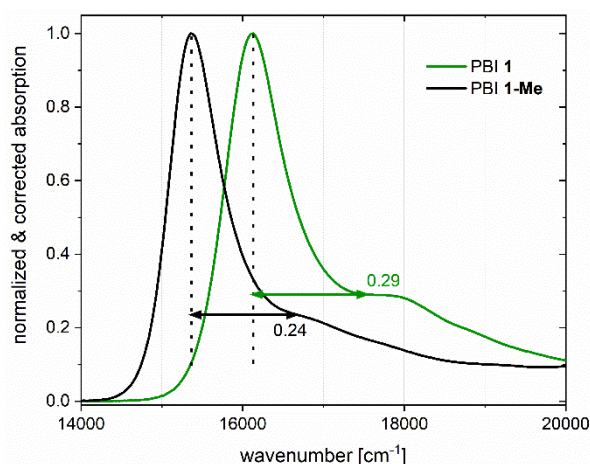


Fig. S5.1. Corrected absorbance for **PBI1** and **PBI1-Me** aggregate in MCH. The measured absorption is divided by the wavenumber and normalized to one to allow extracting the peak ratio. The vertical dashed lines mark the maximum of the absorbance and the horizontal arrow corresponds to the vibrational frequency of the monomer.

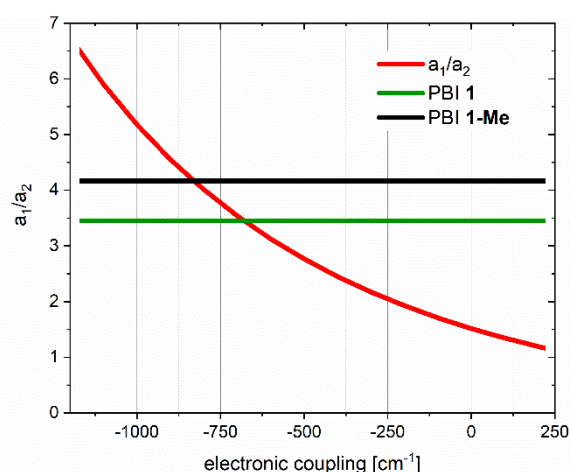


Fig. S5.2. $\frac{a_1}{a_2}$ peak ratio as function of electronic coupling as given by Eq. S5.1 in red. The peak ratios extracted for the two different aggregates are marked as green and black lines. The intersection between the calculated curve and the measured value gives the electronic coupling for the respective aggregate.

Tab. S5.1 Peak ratio as determined from Fig. S5.1. Electronic coupling for the two aggregates according to Fig. S5.2.

	PBI1	PBI1-Me
peak ratio $\frac{a_1}{a_2}$	3.45	4.17
coupling in cm^{-1}	-680	-830
exciton bandwidth	1360	1660

The limit for weak respectively strong electronic coupling is by comparing the exciton bandwidth W with the vibrational frequency $\Delta\nu$. In case that: $W > HR * \Delta\nu$ the aggregate is in the strong coupling regime.[6] The exciton bandwidth for a dimer (delocalization of 2 as for **PBI1**, **PBI1-Me**) is twice the electronic coupling. The product of Huang Rhys factor and

vibrational frequency is: $HR * \Delta\nu = 0.66 * 1330 \text{ cm}^{-1} = 880 \text{ cm}^{-1}$ For both aggregates the exciton bandwidth is larger, therefore, the aggregates are in the limit of the strong coupling regime.

S6. Determination of the coherence length

Upon J-type aggregation, the oscillator strength for the transition from electronic ground to first excited state is redistributed between the 0-0 and the 0-1 vibronic peak in the emission spectra. This yields a change in the vibrational peak ratio of the aggregate spectra compared to the monomer emission spectra. The change is used to determine the coherence length N_{coh} [3, 4]:

$$N_{coh} = HR \frac{a_1}{a_2} \quad (\text{S6.1})$$

where HR is the Huang Rhys factor of the monomer and a_1 and a_2 the vibronic 0-0 and 0-1 transition peak intensity in the emission spectrum.

For the fitting procedure the emission line shape function $g(\nu)$ in dependency of wavenumber ν is used instead of the spontaneous emission spectra $I(\lambda)$ in dependency of the wavelength λ , which is the experimental observable. In our case the emission spectra were measured with a grating monochromator that disperses the spectra proportional to the wavelength. In order to obtain the number of photons in a constant wavenumber interval the emission spectra $I(\lambda)$ has to be divided by the wavenumber squared since $\Delta\nu = \frac{d\nu}{d\lambda} \Delta\lambda = (-) 1/\lambda^2 \cdot \Delta\lambda = \nu^2 \cdot \Delta\lambda$. The line shape function corresponds to the spectrum for stimulated emission while the measured observable is the spontaneous emission. The relation between the Einstein coefficients for stimulated (B_{21}) and spontaneous emission (A_{21}) is given by $B_{21} \propto \frac{A_{21}}{\nu^3}$ [7]. Thus the measured emission has to be divided by the wavenumber cubed to obtain the line shape function. Together with the spectral dispersion of the grating monochromator the measured emission spectra have to be divided by the frequency to the power of five.

$$g_{Em}(\nu) \propto \frac{I(\lambda)}{\nu^5} \quad (\text{S6.2})$$

S6.1 Determination of the Huang-Rhys factor

The procedure for determining the Huang-Rhys factor is based on the model of two shifted harmonic oscillators in the ground and electronically excited state. The vibrational progressions of the ground state absorption and of the emission from the first excited state depend on the shift between the two harmonic potentials along the vibrational normal coordinates. This

shifting is described by the dimensionless Huang-Rhys factor and can be extracted from the progression in the monomer absorption or emission as

$$HR = \left(\frac{a_1}{a_2}\right)^2 \quad (\text{S6.3})$$

with the peak height of the 0→0 transition a_1 and the 0→1 transition a_2 [8].

Often, the progression is described by effective modes. In this case, the area under the peaks has to be considered [9]. This principle also holds for all ratio determinations later on. As we fit the first two peaks of the progression using the same width for the Gaussians, the ratio of the areas are proportional to the height of the Gaussians. In the present case the absorption of the second electronically excited state overlaps with the absorption of the first excited state. Therefore, we use the monomer emission instead of the absorption for the determination of the Huang-Rhys factor, which is in contrast to [10] but equally well suited after appropriate scaling (see Eq. S6.2). The fitting function is

$$f(\nu) = a_1 \cdot \exp\left[-\left(\frac{\nu - \nu_1}{w}\right)^2\right] + a_2 \cdot \exp\left[-\left(\frac{\nu - (\nu_1 - \Delta\nu_{monomer})}{w}\right)^2\right] \quad (\text{S6.4})$$

where ν is the wavenumber, ν_i the spectral position of the i -th maximum and w the width.

Please note that the width is the same for both Gaussians. The results of the fit are listed in Tab. 6.1. The resulting HR factors are 0.67 and 0.66 for **PBI1** and **PBI1-Me**, respectively.

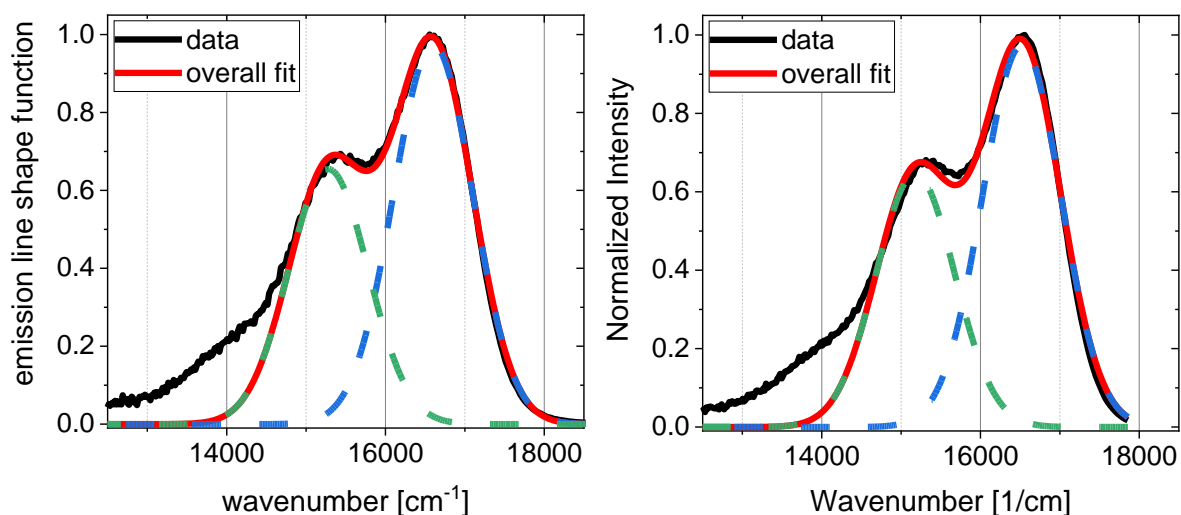


Fig. S6.1. Monomer emission spectra of **PBI1** (left) and **PBI1-Me** (right) scaled with a factor of ν^{-5} and fitted with two Gaussians. The blue and green curve show the individual Gaussian bands.

Tab. S6.1. Fit parameters for monomer emission spectra. Widths of the individual Gaussian bands are set equal.

	PBI1	PBI1-Me
a_1 / arb.units	0.9745	0.9735

a_2 / arb.units	0.6550	0.6466
ν_1 / cm^{-1}	16,600	16,520
$\Delta\nu_{\text{monomer}}$ / cm^{-1}	1,320	1,340
w / cm^{-1}	706.5	698.9
HR	0.67	0.66

S6.2 Coherence length from the vibrational progression in the emission

According to [8], the coherence length can be determined from the aggregate emission spectra by

$$N_{coh} = HR \frac{a_1}{a_2} \quad (\text{S6.5})$$

where a_1 and a_2 are the amplitudes of the 0-0 and 0-1 transitions, respectively.

Fitting the emission with Gaussians strongly depends on applied constraints. Therefore, we compare two methods. The first one is a classical fitting procedure, where the values known from the monomer, i.e., the vibrational frequencies are fixed. The aggregate emission is thereby fitted by two Gaussian bands, see Fig. S6.2:

$$f(\nu) = a_1 \cdot \exp \left[- \left(\frac{\nu - \nu_1}{w} \right)^2 \right] + a_2 \cdot \exp \left[- \left(\frac{\nu - (\nu_1 - \Delta\nu_{monomer})}{w} \right)^2 \right] \quad (\text{S6.6})$$

ν_1 is the wavenumber of the global maximum, w the width of the bands, and $\Delta\nu_{monomer}$ the vibrational frequency of the monomer. The position of the first maximum ν_1 is fixed by hand and $\Delta\nu_{monomer}$ is known from the monomer emission spectrum. The obtained fits are shown Fig. S6.2 while the chosen parameters and the results for a_1 , a_2 , and w are listed in Tab. S6.1 together with N_{coh} calculated by means of Eq. S6.5.

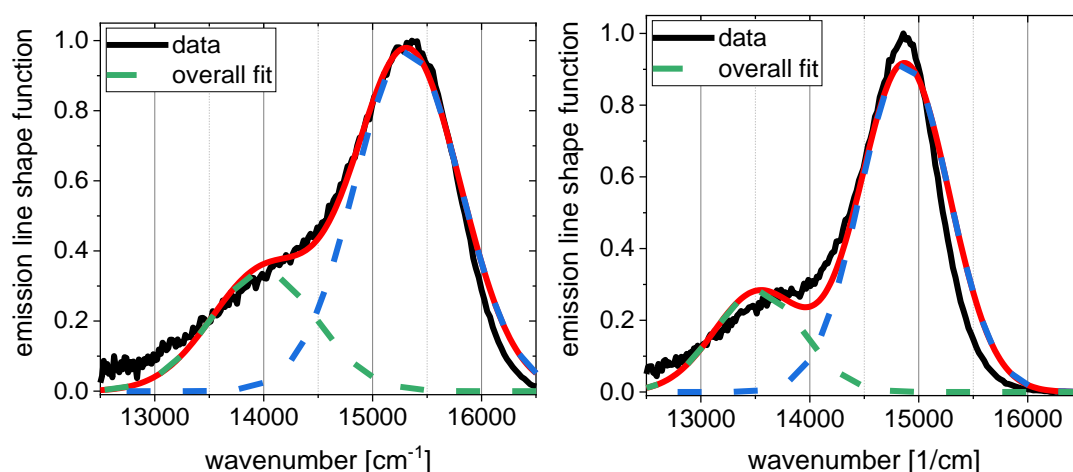


Fig. S6.2: Fitted aggregate emission line shape function of **PBI1** (left) and **PBI1-Me** (right). The green and the blue curves show the individual Gaussian bands accumulating to the overall fit. The position of the global maximum is fixed by hand and the position of the next progression contribution is determined by the global maximum position and the vibrational frequency in monomer emission (1,320 cm⁻¹ and 1,340 cm⁻¹).

In the second method, we determine a_1 at the global maximum and a_2 from the signal at $\nu_2 = \nu_1 - \Delta\nu_{monomer}$. The results for a_2 and N_{coh} are again given in Tab. S6.1.

Table S6.2. Results from evaluating the aggregate emission spectra and resulting coherence lengths.

method	parameter	PBI1	PBI1-Me
	HR	0.67	0.66
	$\Delta\nu_{\text{monomer}} / \text{cm}^{-1}$	1,320	1,340
fit	$a_1 / \text{arb.units}$	0.9708	0.9165
	$a_2 / \text{arb.units}$	0.3383	0.2798
	ν_1 / cm^{-1}	15,320	14,870
	w / cm^{-1}	688.9	576.7
	N_{coh}	1.9	2.2
value at $\nu_2 = \nu_1 - \Delta\nu_{\text{mono}}$	$a_1 / \text{arb.units}$	0.9800	0.9800
	$a_2 / \text{arb.units}$	0.3210	0.2504
	N_{coh}	2.0	2.6

For the coherence length of **PBI1** we obtain either 1.9 or 2.0, within the experimental error these two values coincide and thus 2 is taken as coherence length. In the case of **PBI1-Me** slightly larger values of 2.2 and 2.6 are obtained such that we give the coherence length between 2 and 3. However, the value is only slightly larger than for **PBI1** such that we conclude that there is no qualitative difference between the two aggregates with regard to the expected mechanisms for exciton transfer.

The aggregates of **PBI1** and **PBI1-Me** exhibit an appreciable high quantum yield Φ_{FI} (emission maximum) of 64% (653 nm/15300 cm^{-1}) and 74% (672 nm/14900 cm^{-1}), respectively.

S6.3 Coherence length from motional narrowing

In aggregates the line width of the absorption spectra is narrowed compared to the monomer by a factor of $N_{coh}^{1/2}$ due to motional narrowing. The delocalization length then reads [11]

$$N_{coh} = \left(\frac{w_M}{w_A} \right)^2 \quad (\text{S6.7})$$

where w_M and w_A are the line widths of the monomer and aggregate absorption bands, respectively. However, the vibronic bands exhibit asymmetric shapes due to the superposition of several vibronic progressions. For this reason only the long wavelength wing of the 0-0 transition is evaluated. The line widths of the monomer and aggregate absorption are determined by fitting this wing with a Gaussian:

$$f(\nu) = a_1 \cdot \exp \left[- \left(\frac{\nu - \nu_1}{w} \right)^2 \right] \quad (\text{S6.8})$$

where ν is the wavenumber, ν_1 the spectral position of the global maximum and w the width.

Tab. S6.3. Fit parameters for the monomer and aggregate absorption spectra. Only the low energy wing of the global maximum is fitted.

	PBI1	PBI1-Me
w_M / cm^{-1}	694.4	630.0
w_A / cm^{-1}	494.2	398.9
N_{coh}	2.0	2.5

The fitted parameters are given in Tab. S6.3 and the corresponding fits are displayed in Fig. S6.3 and S6.4. The resulting coherence lengths are 2.0 (**PBI1**) and 2.5 (**PBI1-Me**). These coherence lengths are in excellent accordance with the ones obtained by evaluating the vibrational progression of the emission spectra.

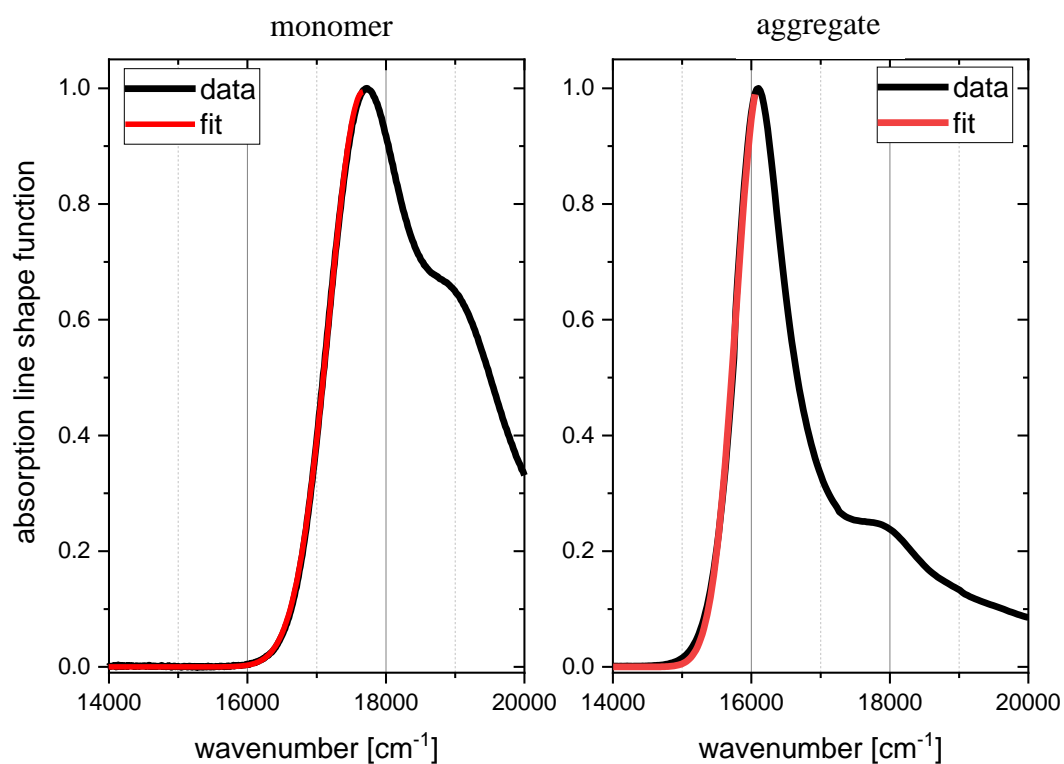


Fig. S6.3: Absorption line shape function of monomer (left panel) and aggregate (right panel) of **PBI1** and their corresponding fits for the rising edge. The spectra are fitted with one Gaussian only for $\nu < \nu_1$, where ν_1 is the wavenumber of the first maximum.

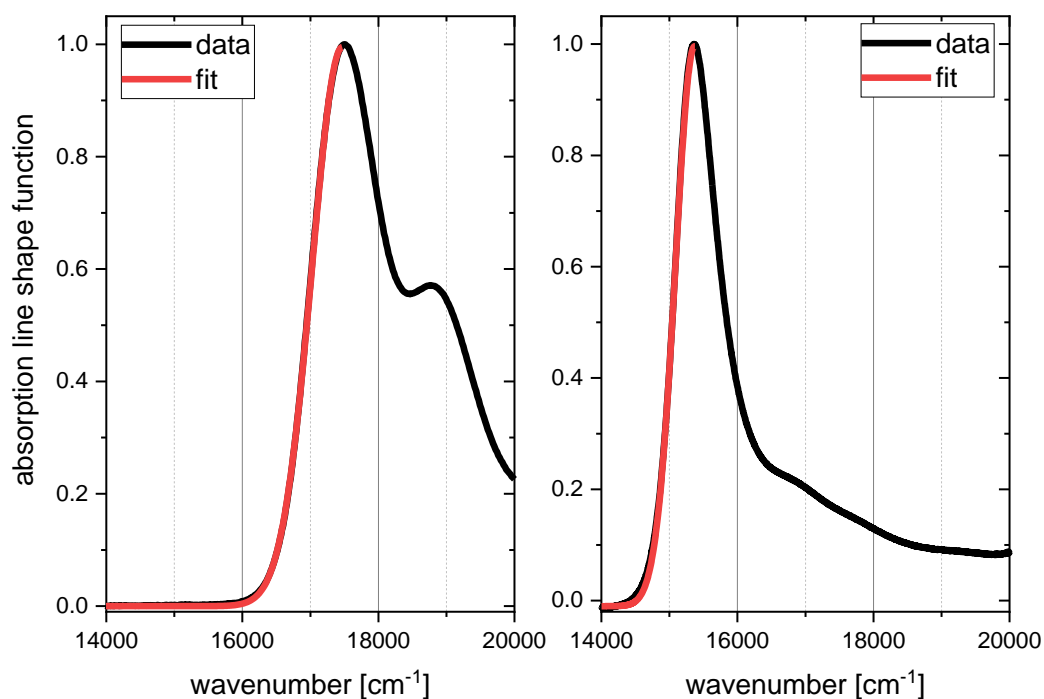


Fig. S6.4: Absorption line shape function of monomer (left panel) and aggregate (right panel) of **PBI1-Me** and their corresponding fits for the rising edge. The spectra are fitted with one Gaussian only for $\nu < \nu_1$, where ν_1 is the wavenumber of the first maximum.

S7. Comparison of transient spectra

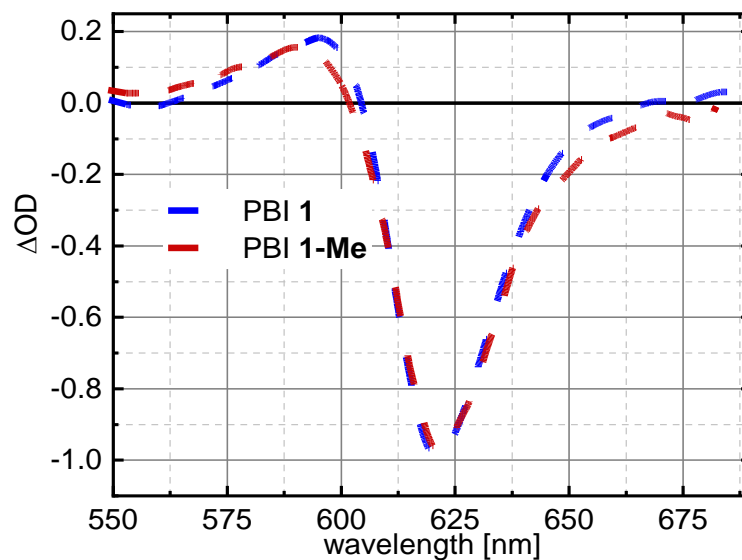


Fig. S7.1 Normalized transient absorption spectra at 100 fs with minima shifted to the **PBI1** minimum. The transient absorption spectra of both aggregates are almost identical in shape as the exemplary comparison in Fig. S7.1 for a delay time of 100 fs shows.

S8. Exciton diffusion properties

S8.1 Determination of the excitation density

The exciton density is calculated with the following expression:

$$n_{ex}(x, y) = \frac{E}{hf} \cdot \frac{2 \cdot (1 - T)}{\pi \sigma_x \sigma_y} \cdot \exp\left(-\frac{2x^2}{\sigma_x^2} - \frac{2y^2}{\sigma_y^2}\right) \quad (\text{S8.1})$$

where E is the pump pulse energy, $\sigma_{x,y}$ the size of the pump beam in x respectively y direction taking the ellipticity of the pump focus into account. Typical values are $\sigma_x = 330\text{-}400 \mu\text{m}$ and $\sigma_y = 220\text{-}270 \mu\text{m}$. T is the fraction of transmitted photons and takes the broad band excitation of the pump pulse and the changes of the sample absorption in the spectral range of the excitation pulse into account. T is calculated as the spectral integral of the product of the sample transmission and the wavelength dependent excitation spectrum normalized to the total number of pump photons. The pump spectrum is centered at 600 nm with a FWHM of about 50 nm.

As the probe focus is much smaller than the pump focus only the central part of the radial excitation density distribution is probed by the probe pulse. The probed exciton density is calculated by weighting the spatial exciton population with the probe photon density distribution:

$$\begin{aligned} n_{detected} &= \frac{E}{hf} \cdot \frac{2 \cdot (1 - T)}{\pi \sigma_x \sigma_y} \\ &\cdot \int_{-\infty}^{\infty} \int_{-\infty}^{\infty} \frac{2}{\pi S_x S_y} \cdot \exp\left(-\frac{2x^2}{\sigma_x^2} - \frac{2x^2}{S_x^2}\right) \\ &\cdot \exp\left(-\frac{2y^2}{\sigma_y^2} - \frac{2y^2}{S_y^2}\right) dx dy \end{aligned} \quad (\text{S8.2})$$

$$= \frac{E}{hf} \cdot \frac{2 \cdot (1 - T)}{\pi \sigma_x \sigma_y S_x S_y} \cdot h_x \cdot h_y \quad (\text{S8.3})$$

with the size of the probe focus in x- and y-direction S_x and S_y and

$$h_i = \sqrt{\frac{1}{\frac{1}{\sigma_i^2} + \frac{1}{S_i^2}}} \quad (\text{S8.4})$$

Typical dimensions of the probe focus are $S_x = 130 \mu\text{m}$ and $S_y = 160 \mu\text{m}$. The relative exciton density, i. e., number of excitons per molecule then reads

$$n_{rel} = \frac{n_{detected}}{n_{molecules}} = \frac{n_{detected}}{c_{molecules} \cdot N_A} \quad (\text{S8.5})$$

The negative signal of the spectra at early times is used to analyze if the densities are consistent compared to each other. Single densities are corrected to the linear dependence between signal and exciton density if the deviation is severe. These deviations result probably from experimental errors in determining the spot sizes. We further adapt the exciton densities slightly during the global fitting procedure described in the next subsection. The final exciton densities are 3.10%, 1.59%, 0.97%, 0.53%, 0.20% (**PBI1**) and 3.21%, 2.29%, 1.38%, 0.64%, 0.34% (**PBI1-Me**)

S8.2 Determination of the diffusion constant

In order to fit our model to the data we integrated ΔOD over the negative part of the spectrum. Fig. S8.1 shows the integration area. The resulting time traces $\Delta OD(t)$ for different relative exciton densities are analyzed by a global fit which minimizes the RMS for all measurements simultaneously. The fitted model function is based on Eq. 2 of the manuscript and represents a combination of a mono-exponential exciton decay and exciton-exciton annihilation. It reads:

$$\Delta OD(t) = \frac{a \cdot n_0 \cdot \exp\left(-\frac{t}{\tau}\right)}{1 + n_0 \cdot \sqrt{2 \cdot D \cdot \tau} \cdot \operatorname{erf}\left(\frac{t}{\tau}\right)}, \quad (\text{S8.2})$$

where a is the signal amplitude parameter, n_0 the initial relative exciton density, D the diffusion constant in sites^2/ps and τ the lifetime without annihilation.

The fit uses the known relative exciton densities and determines only one parameter for the signal amplitude and one diffusion constant for all measurements. If the fit was satisfactory, we further optimized it with the relative exciton density as free parameter and with the fitted intensity parameter and annihilation rate constant as starting parameters. The relative exciton densities must not change significantly ($< 10\%$). This way, we can account for possible systematic errors in the determination of the exciton density. Fig. S8.1 shows the results of the fitting procedure. The final relative exciton densities for each measurement can be found in the caption and at the end of the previous subsection. The obtained diffusion constants are 20 sites^2/ps for **PBI1-Me** and 12 sites^2/ps for **PBI1**.

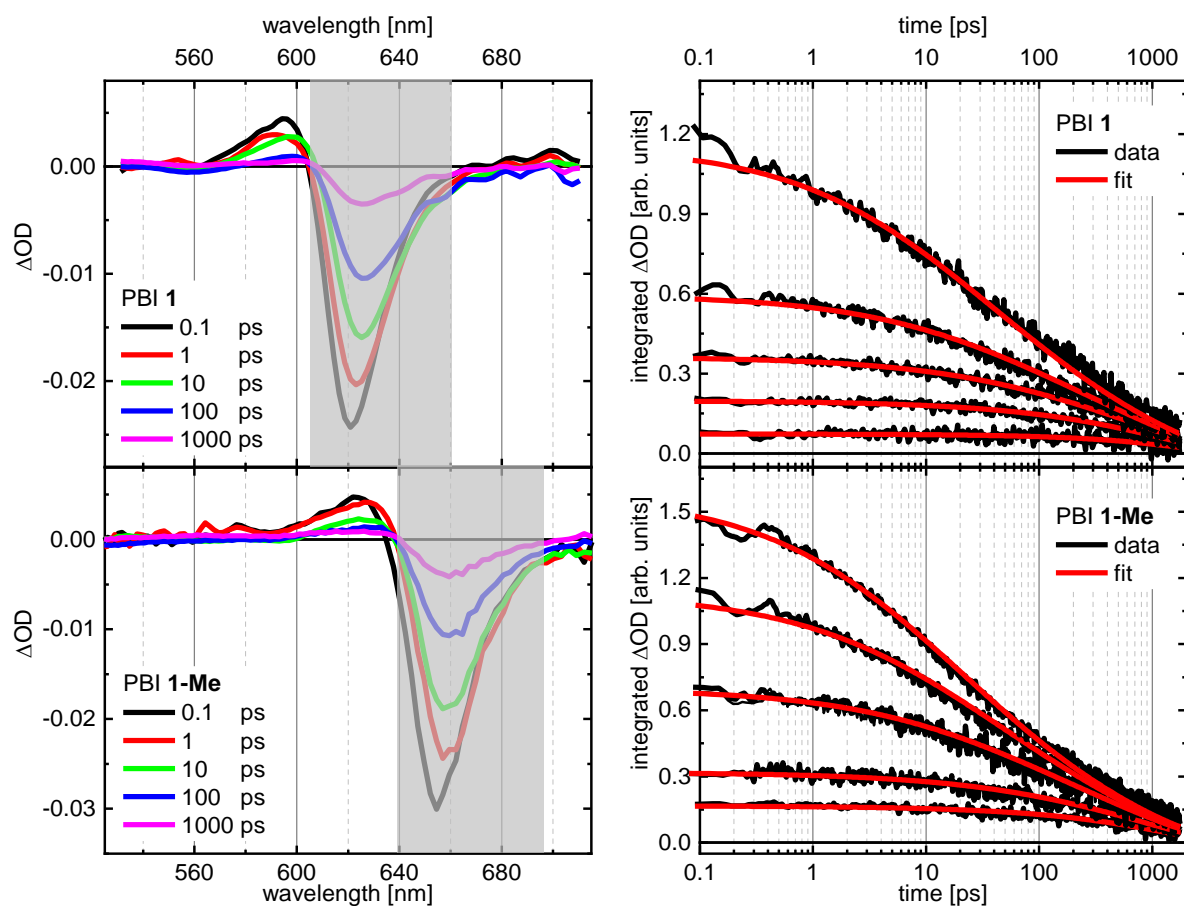


Fig. S8.1 Left panels: Typical time dependent transient absorption spectra for a relative exciton density of 1.61 % and 1.38 % for **PBI1** (upper panel) and **PBI1-Me** (lower panel), respectively. The grey area shows the integration window for the analysis of the time-dependent behavior of the signal as depicted in the right panel. Right panels: Integrated signal curves corresponding to different relative exciton densities. These are: 0.20 %, 0.53 %, 0.97 %, 1.59 % and 3.10 % for **PBI1**; 0.34 %, 0.64 %, 1.38 %, 2.29 % and 3.21 % for **PBI1-Me**. The red curves show the results of a global fit which is based on a mono-exponential decay and exciton-exciton annihilation.

S9. Lifetime measurements

The fluorescence lifetime of the samples were determined by streak camera measurements (Streakscope C10627, Hamamatsu). Ultrashort excitation pulses with a center wavelength of 560 nm are applied. Their scattered light is blocked by a RG645 filter in front of the entrance slit of the streak camera.

The samples were diluted eight times (**PBI1-Me**) or four times (**PBI1**) compared to the concentration of the transient absorption measurements in order to avoid self-absorption. For **PBI1** there is a small monomer contribution visible in the absorption spectra. By excitation at 560 nm we ensured that the monomer is not excited and in the emission spectrum of the diluted **PBI1** sample there is no contribution of the monomer present. For **PBI1-Me** dilution is uncritical and does not lead to a monomer contribution as the association constants K_N , and K_E are much higher. The fluorescence spectra obtained by the streak camera measurements reproduce the spectra from the static fluorescence measurements on the aggregates. The emission lifetime is independent on the emission wavelength, which ensured that no additional species is present. In order to fit the fluorescence lifetime the spectra are integrated (330-700 nm) and fitted by an exponential decay convoluted with the Gaussian shaped instrument response function (FWHM 200 ps), see Fig. S9. No deviations from a mono-exponential decay are observed and the statistical error of the fitted lifetimes is between 0.6 and 1 %.

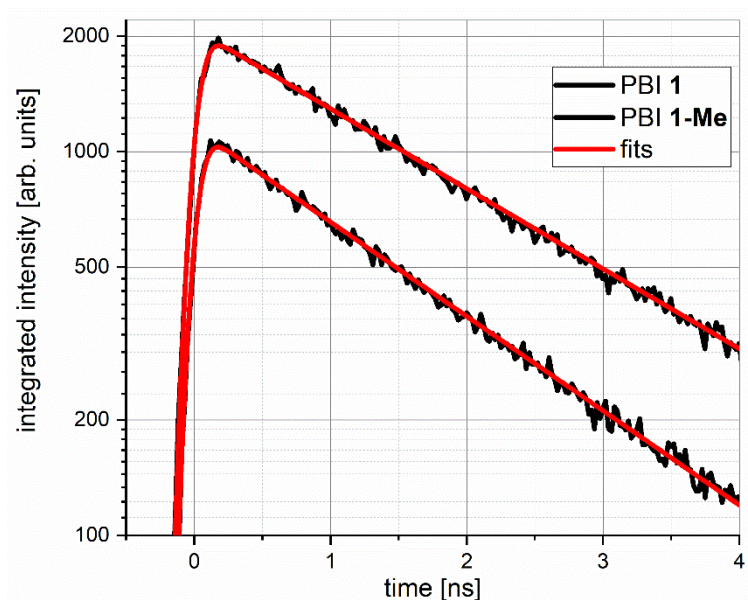


Fig. S9. Spectrally integrated fluorescence decay. The time resolution of the streak camera setup is 200 ps (FWHM of the instrument response function). The obtained fluorescence lifetimes are 2080 ps for **PBI1** and 1770 ps for **PBI1-Me**. The overall intensity is arbitrary and chosen to present the data in a clear fashion.

S10. Spectral overlap of absorption and emission

In order to get an estimate for the scaling of the exciton diffusion constant we consider Förster transfer for the individual steps. Applying the dipole-dipole approximation for the interaction between two adjacent sites the transfer rate for an individual step reads

$$k_{FT} = \frac{1}{\tau_{\text{rad}}} \cdot \left(\frac{R_0}{R_{DA}} \right)^6, \quad (\text{S10.1})$$

where R_{DA} is the distance between the two sites and τ_{rad} the radiative life time. R_0 is a characteristic length scale for the Förster transfer and gives the distance between two sites where the radiative decay has the same probability as energy transfer. The Förster radius is given by

$$R_0 = \left(\frac{9000 f^2 \ln(10)}{128 \pi^5 N_A n^4} \cdot J \right)^{1/6} \quad \text{with } J = \frac{\int \varepsilon(\nu) F(\nu) \nu^4 d\nu}{\int F(\nu) d\nu} \quad (\text{S10.2})$$

The parameter f^2 accounts for the relative orientation of the two partners, n is the refractive index and N_A the Avogadro constant. Here, the important variable is the spectral overlap integral J , which describes the overlap of the extinction of the acceptor molecule and the emission of the donor molecule in dependency of the wavenumber ν . Fig. S10.1 shows the extinction and emission spectra and the overlap area which is colored in purple.

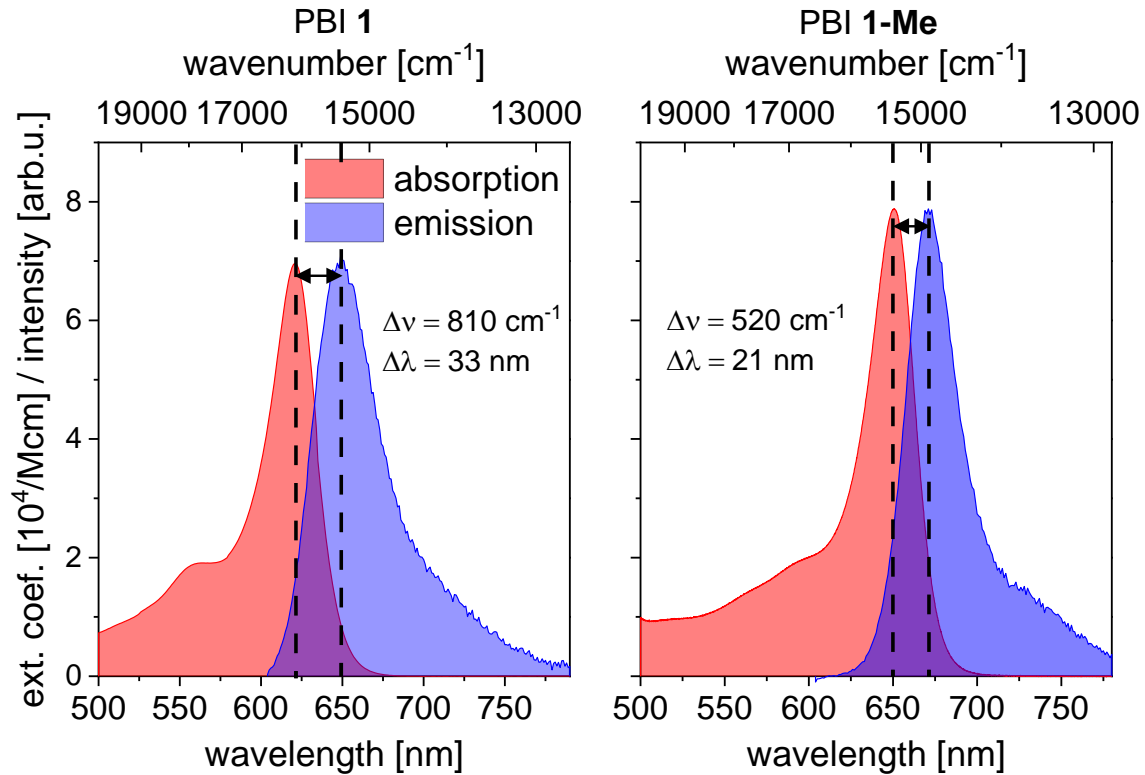


Fig. S10.1. Extinction coefficient and fluorescence intensity in the overlap area. The fluorescence is scaled to the maximum of the extinction.

The largest overlap integral is observed for **PBI1-Me** as can be better seen by plotting the spectral overlaps together, see Fig. S10.2

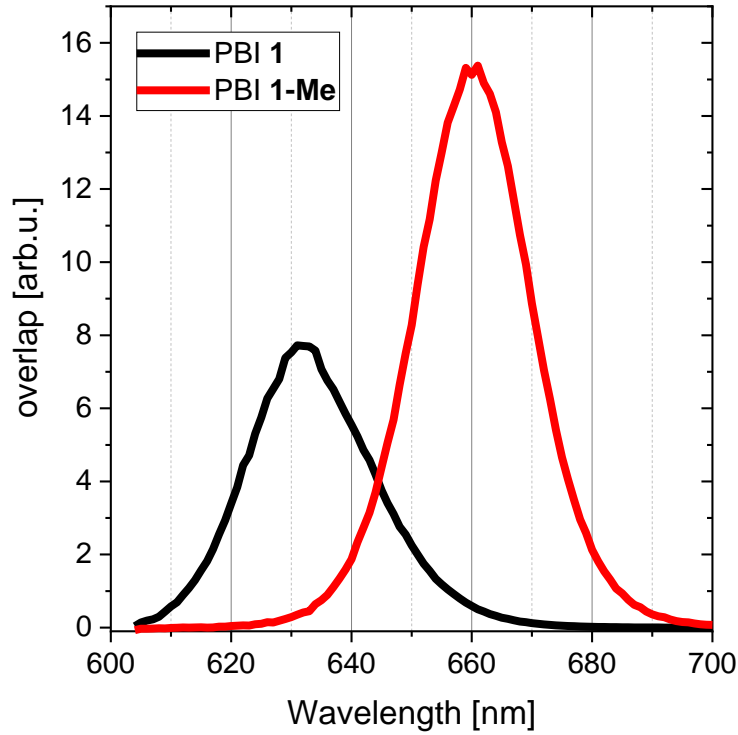


Fig. S10.2. Product of absorption and fluorescence ($\epsilon F\nu^4$) according to Eq. S9.2.

The overlap integral of **PBI1-Me** is 1.8 times larger than the integral of **PBI1**.

The diffusion constant for a 1D motion is calculated by the transfer rate of an individual step by [12]:

$$D_{1D} = 0.5 \cdot k_{FT} \cdot R_{DA}^2 \propto J \quad (\text{S10.3})$$

Thus the 1D diffusion constant is proportional to the spectral overlap integral J . Förster theory makes use of the dipole-dipole approximation, which is based on the assumption that the distance between two dipoles is much larger than the spatial extent of the dipoles. The assumption breaks down for closely stacked aggregates and Förster theory overestimated the transfer considerably [13]. However, the principal scaling of the diffusion constant with the overlap integral should persist such that the relative exciton diffusion constant of two similar aggregates as considered here should also scale with the overlap integrals.

Literature

- [1] T. Wilhelm, J. Piel, and E. Riedle, *Opt. Lett.*, 1997, **22**, 1494–1496.
- [2] R. F. Goldstein and L. Stryer, *Biophys. J.*, 1986, **50**(4), 583–599.
- [3] K. A. Kistler, C. M. Pochas, H. Yamagata, S. Matsika, and F. C. Spano, *J. Phys. Chem. B*, 2012, **116**(1), 77–86.
- [4] F. Spano, *J. Chem. Phys.*, 2005, **122**(23), 234701.
- [5] H. Haken and H. Wolf, *Molekülphysik und Quantenchemie: Einführung in die experimentellen und theoretischen Grundlagen*, Springer, 5 ed., 1992.
- [6] F. C. Spano, *Acc. Chem. Res.*, 2010, **43**(3), 429–439.
- [7] S. Strickler and R. Berg, *J. Chem. Phys.*, 1962, **37**(4), 814–820.
- [8] F. C. Spano and H. Yamagata, *J. Phys. Chem. B*, 2011, **115**(18), 5133–5143.
- [9] D. Ambrosek, A. Köhn, J. Schulze, and O. Kühn, *J. Phys. Chem. A*, 2012, **116**(46), 11451–11458.
- [10] A. T. Haedler, K. Kreger, A. Issac, B. Wittmann, M. Kivala, N. Hammer, J. Koehler, H.-W. Schmidt, and R. Hildner, *Nat.*, 2015, **523**(7559), 196–199.
- [11] E. Knapp, *Chem. Phys.*, 1984, **85**, 73–82.
- [12] S. Chandrasekhar, *Rev. Mod. Phys.*, 1943, **15**(1), 0001–0089.
- [13] D. Beljonne, C. Curutchet, G. D. Scholes, and R. J. Silbey, *J. Phys. Chem. B*, 2009, **113**(19), 6583–6599.